PHOTONICS Research

Impact of carrier transport on the performance of QD lasers on silicon: a drift-diffusion approach

Marco Saldutti,* Alberto Tibaldi, Federica Cappelluti, and Mariangela Gioannini

Department of Electronics and Telecommunications, Politecnico di Torino, Turin 10129, Italy
**Corresponding author: mariangela.gioannini@polito.it*

Received 3 April 2020; revised 22 June 2020; accepted 23 June 2020; posted 23 June 2020 (Doc. ID 394076); published 31 July 2020

The operation of quantum dot lasers epitaxially grown on silicon is investigated through a quantum-corrected Poisson-drift-diffusion model. This in-house developed simulation framework completes the traditional rate equation approach, which models the intersubband transitions involved into simultaneous ground-state and excited-state lasing, with a physics-based description of carrier transport and electrostatic effects. The code is applied to look into some of the most relevant mechanisms affecting the lasing operation. We analyze the impact of threading dislocations on non-radiative recombination and laser threshold current. We demonstrate that asymmetric carrier transport in the barrier explains the ground-state power quenching above the excited-state lasing threshold. Finally, we study p-type modulation doping and its benefits/contraindications. The observation of an optimum doping level, minimizing the ground-state lasing threshold current, stems from the reduction of the electron density, which counteracts the benefits from the expected increase of the hole density. This reduction is due to electrostatic effects hindering electron injection.

https://doi.org/10.1364/PRJ.394076

1. INTRODUCTION

Energy-efficient and low-cost silicon photonics technologies for CMOS-compatible optical interconnects are a very attractive solution for high-capacity, high-speed data links in data centers and supercomputers. In this context, quantum dot (QD) laser diodes, already considered the most promising lasers for optical communications [1], are attracting strong interest for direct epitaxial growth on silicon. This monolithic integration [2–4] is the ultimate solution to minimize the complexity and cost of the fabrication process and improve the integration density of the silicon photonic integrated circuit. However, the mismatch in the lattice constant and thermal expansion coefficients causes the generation of threading dislocations (TDs), which act as non-radiative recombination centers and degrade the laser performance. Despite the significant progress made recently [5–8], the achievable TD density is still around 10^5–10^6 cm^{-2}. At such high densities, quantum well (QW) lasers either show very poor performances or do not even lase [9]. On the contrary, QDs have proved to be more tolerant to TDs, due to 3D carrier localization within the QDs [10,11].

Apart from this feature, QD lasers on Si share several similarities with ordinary QD laser diodes on GaAs. Among these, we cite the double-state lasing from both ground state (GS) and excited state (ES) and the fast hole thermalization in the QD confined states of the valence band [12,13]. A detrimental effect related to double-state emission is the GS power quenching taking place above the ES threshold [14–16]. The hole thermalization, which increases the laser threshold and reduces the differential gain, is usually cured via p-type modulation doping [17–19], which has been recently employed also for QD lasers on silicon [20]. Experimental results have demonstrated that an optimum doping level exists [20], as an excessive doping can degrade the GS optical power and the threshold current. This effect is a matter of debate and has been attributed to different phenomena such as the enhanced free carrier absorption [18] or the increase in the carrier scattering rate and defect-assisted recombination with the doping level [20].

In order to devise a proper strategy to overcome these limitations, modeling can be an instrumental platform to achieve deeper understanding of the device operation. In this context, most of the literature relies on (often ambipolar) lumped rate equations describing the interaction of carriers and photons in each energy state. Even though such approaches provide an appropriate picture of the intersubband interactions, they reduce the model of the separate-confinement heterostructure (SCH) to phenomenological capture terms [11,14], neglecting carrier transport and electrostatic effects. This paper aims to fill this gap by investigating the role of transport and electrostatics in the peculiar features of QD-on-Si lasers, with the help of a quantum-corrected physics-based semiclassical model [21–23]. The model is applied to characterize the steady-state performance of QD-on-Si lasers with InAs/GaAs self-assembled QDs emitting at 1.3 μm, at ambient temperature. Specifically, we study the impact of TDs on laser power versus current

characteristics, the role of carriers transport in the competition between GS and ES lasing, and the physics behind the existence of an optimum p-type modulation doping level that minimizes the laser threshold current.

2. METHOD

A. Device under Study

A schematic drawing of the epitaxial structure of the investigated QD lasers is illustrated in Fig. 1. The structure is similar to others reported in the literature [24,25]. In these devices, the layers grown immediately above the silicon substrate act as buffers and dislocation filters reducing the density of TDs in the n-type cladding and SCH region. The n-type electrical contact is positioned on top of a GaAs n-doped buffer layer, thus avoiding carrier injection through the much more defective layers located below. For this reason, we have not simulated transport through the silicon substrate and buffer and we have assumed that electrons are directly injected through the 500 nm n-doped GaAs layer. The active region includes five layers of InAs QDs, each grown in a 11.5-nm-thick $In_{0.15}Ga_{0.85}As$ QW, thus forming a dot-in-a-well (DWELL) structure. In each of the 37.5-nm-thick GaAs spacers separating a DWELL layer from another, the central 10-nm-thick region can either be intrinsic or p-type modulation doped.

B. Model

The simulation framework consists of an in-house developed Poisson-drift-diffusion system augmented with carrier and photon rate equations of the localized states. The code requires as input a detailed description of the layer stack (material composition, doping) and QD characteristic parameters listed in Table 1. In this work, these parameters have been taken from our previous work [14] or extracted from literature experimental data representative of QD lasers on silicon.

Figure 2 shows the calculated energy band diagram under thermodynamic equilibrium for the device sketched in Fig. 1.

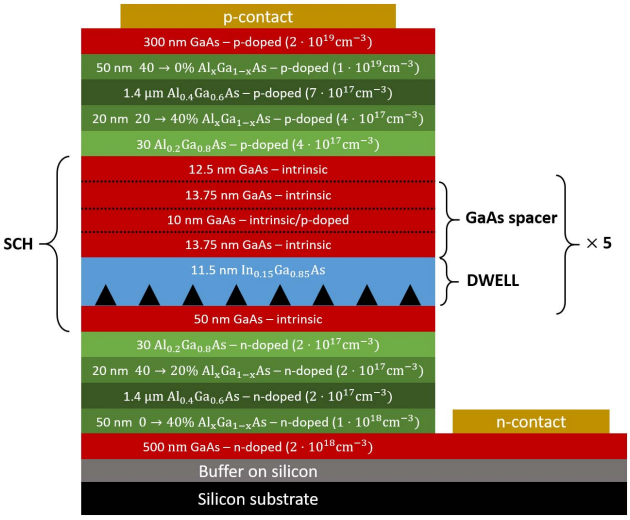

Fig. 1. Schematic representation of the epitaxial structure of the studied QD lasers, similar to those in Refs. [24,25]. The growth direction is from the bottom to the top.

Table 1. Simulation Parameters

Parameters	Values
ΔE_n^k, k = WL, ES, GS [meV]	177.7, 30, 41.1 [14]
ΔE_p^k, k = WL, ES, GS [meV]	166.3, 25, 25 [14]
$\tau_{n,\mathrm{CAP}}^{B\to\mathrm{WL}}$, $\tau_{n,\mathrm{CAP}}^{\mathrm{WL}\to\mathrm{ES}}$, $\tau_{n,\mathrm{CAP}}^{\mathrm{ES}\to\mathrm{GS}}$ [ps]	0.1, 1, 1 [26]
$\tau_{p,\mathrm{CAP}}^{B\to\mathrm{WL}}$, $\tau_{p,\mathrm{CAP}}^{\mathrm{WL}\to\mathrm{ES}}$, $\tau_{p,\mathrm{CAP}}^{\mathrm{ES}\to\mathrm{GS}}$ [ps]	0.1, 0.1, 0.1 [26]
τ_{rad}^k, k = WL, ES, GS [ns]	1, 1, 1 [11,22]
$\tau_{n,\mathrm{SRH}}^k$, k = ES, GS [ns]	1, 1 [11,22]
$\tau_{p,\mathrm{SRH}}^k$, k = ES, GS [ns]	1, 1 [11,22]
QD sheet density $N_{\mathrm{QD},i}$ [cm^{-2}]	4.9×10^{10}
GS (ES) degeneracy μ_{GS} (μ_{ES})	2 (4)
Gain coefficient G_0^{GS} (G_0^{ES}) [cm^{-1}]	433 (779.4)
Electron (hole) effective mass m_n^* (m_p^*) [m_0]	0.054 (0.49)
Optical confinement factor Γ_i	~2%
Intrinsic loss α_i [cm^{-1}]	5
Waveguide width [μm]	3.5
Facet reflection coefficient	0.32
Spontaneous emission factor β_{sp}	10^{-4}
Group index	3.56
GaAs D_n, D_p [cm$^2\cdot$s^{-1}]	221, 10
$In_{0.15}Ga_{0.85}As$ D_n, D_p [cm$^2\cdot$s^{-1}]	181, 10
Temperature [K]	300

The quantum-corrected carrier continuity equations are formulated within a drift-diffusion-Poisson formalism as

$$\frac{\partial n}{\partial t}=\frac{1}{q}\frac{\partial J_n}{\partial x}-U^B-\sum_i\left(R_{n,\mathrm{CAP}}^{B\to\mathrm{WL},i}-R_{n,\mathrm{ESC}}^{\mathrm{WL},i\to B}\right)\delta(x-x_i), \quad (1)$$

$$\frac{\partial^2\phi}{\partial x^2}=-\frac{q}{\epsilon}\left[p-n+N+\sum_{k,i}(p_{k,i}-n_{k,i})\delta(x-x_i)\right], \quad (2)$$

where x is the growth direction of Fig. 1; J_n is the electron current density, U^B is the net band-to-band recombination rate including Shockley–Read–Hall (SRH) and radiative processes, and N is the net doping. $R_{n,\mathrm{CAP}}^{B\to\mathrm{WL},i}$ and $R_{n,\mathrm{ESC}}^{\mathrm{WL},i\to B}$ are the capture and escape rates between the barrier and the i-th QD layer

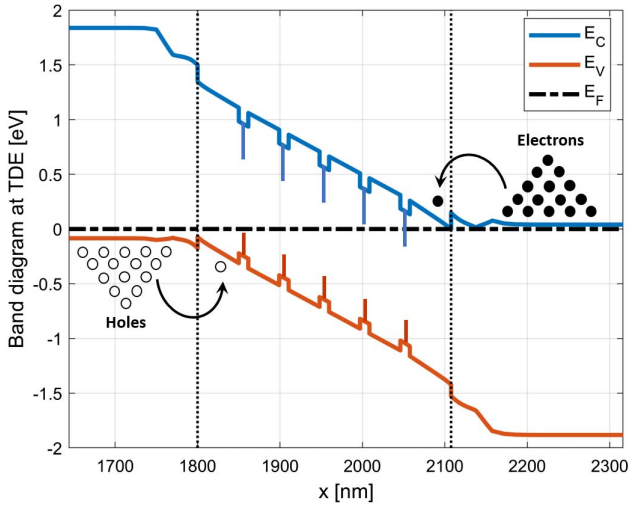

Fig. 2. Band diagram at thermodynamic equilibrium, with the conduction band (blue), the valence band (red), and the Fermi level (dashed, black). The dotted, vertical lines delimit the SCH region.

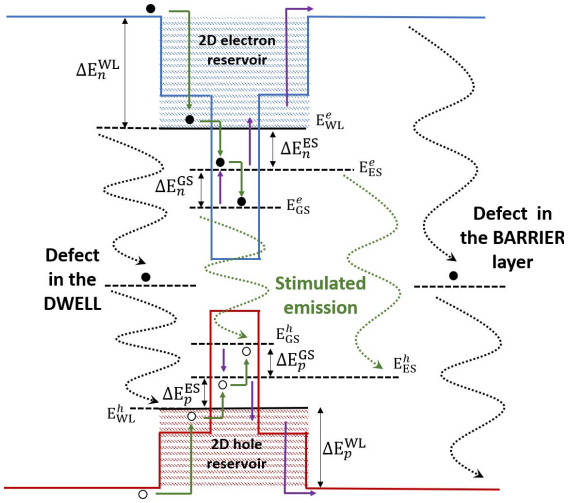

Fig. 3. Schematic representation of the QD energy states and inter-subband transitions.

(located in the node x_i), respectively. For the sake of brevity, drift-diffusion and carrier rate equations are reported here for electrons only, but a similar set of equations is implemented also for holes.

Figure 3 illustrates the model employed for the dynamics in each QD layer. The rate equations governing the electron dynamics in the ith QD layer are

$$\frac{\partial n_{k,i}}{\partial t} = (R_{n,\mathrm{CAP}}^{k+1,i\to k,i} - R_{n,\mathrm{ESC}}^{k,i\to k+1,i}) - (R_{n,\mathrm{CAP}}^{k,i\to k-1,i} - R_{n,\mathrm{ESC}}^{k-1,i\to k,i}) - U^{k,i} - R_{\mathrm{st}}^{k,i}, \tag{3}$$

where $U^{k,i}$ accounts for SRH and radiative recombination and $R_{\mathrm{st}}^{k,i}$ is the stimulated recombination rate. $R_{n,\mathrm{CAP}}^{k,i\to k-1,i}$ and $R_{n,\mathrm{ESC}}^{k-1,i\to k,i}$ are the capture and escape rates between the kth and $(k-1)$th states with $k = B, \mathrm{WL}, \mathrm{ES}$ and $k-1 = \mathrm{WL}, \mathrm{ES}, \mathrm{GS}$, computed as in Refs. [21,27], where WL indicates the wetting layer state including both the 2D well states and the upper continuum of the QDs. The capture rate depends on the capture time ($\tau_{n,\mathrm{CAP}}^{k\to k-1}$) from the state with higher energy (k) to the state with lower energy ($k-1$), whereas the escape rate is dependent on the escape time that leads the system to equilibrium in absence of any injection current or recombination rate [21]. These equations put in relation the 3D carrier volume densities (n, p) with the electrostatic potential ϕ and the sheet carrier density $(n_{k,i}, p_{k,i})$ of the kth QD energy level of the ith QD layer.

The net recombination rate $U^{k,i}$ is given by $U^{k,i} = U_{\mathrm{rad}}^{k,i} + U_{\mathrm{SRH}}^{k,i}$. Here, $U_{\mathrm{rad}}^{k,i}$ is the net radiative recombination rate modeled as

$$U_{\mathrm{rad}}^{k,i} = B_{\mathrm{rad}}^{k}(n_{k,i}p_{k,i} - n_{k0,i}p_{k0,i}), \tag{4}$$

where $n_{k0,i}$ and $p_{k0,i}$ are the electron and hole sheet densities in the kth energy level at thermal equilibrium, respectively, and B_{rad}^{k} is a radiative recombination coefficient related to the radiative time τ_{rad}^{k} [21]. The net SRH recombination rate is modeled as

$$U_{\mathrm{SRH}}^{k,i} = \frac{n_{k,i}p_{k,i} - n_{k0,i}p_{k0,i}}{\tau_{n,\mathrm{SRH}}^{k}(p_{k,i} + p_{k0,i}) + \tau_{p,\mathrm{SRH}}^{k}(n_{k,i} + n_{k0,i})}, \tag{5}$$

where $\tau_{n,\mathrm{SRH}}^{k}$ and $\tau_{p,\mathrm{SRH}}^{k}$ are SRH lifetimes for electrons and holes, respectively. The SRH lifetime in the barrier and DWELL ($k = B, \mathrm{WL}$) is reduced by the presence of TDs according to [28,29]

$$\frac{1}{\tau_{n(p),\mathrm{SRH}}} = \frac{1}{\tau_{n(p),\mathrm{SRH}}^{0}} + \frac{\pi^3 D_{n(p)}\mathrm{TDD}}{4}, \tag{6}$$

with $\tau_{n(p),\mathrm{SRH}}^{0}$ being the typical (doping-dependent) lifetime of dislocation free GaAs [30], and TDD the TD density. The WL stimulated emission rate is assumed to be negligible. The GS and ES stimulated emission rates are given by

$$R_{\mathrm{st}}^{k,i} = v_g G_0^k \Gamma_i(\rho_n^{k,i} + \rho_p^{k,i} - 1)S^k, \tag{7}$$

where $k = \mathrm{ES}, \mathrm{GS}$, S^k is the photon density emitted by the GS or ES ($k = \mathrm{GS}, \mathrm{ES}$), v_g is the group velocity, and $\rho_{n(p)}^{k,i}$ is the occupation probability of electrons (holes) kth energy level of the ith QD layer. The coefficient G_0^k is the saturated material gain (i.e., the material gain if the electron and hole kth state was fully filled) of the QD layer. Γ_i is the optical confinement factor of the TE fundamental mode in the ith QD layer and it has been computed from the fundamental TE mode profile of the epitaxial structure with no optical gain. The rate equation for the photon density S^k is governed by

$$\frac{\partial S^k}{\partial t} = \beta_{\mathrm{sp}} R_{\mathrm{sp}}^{k} + v_g G_k^{\mathrm{mod}} S^k - \frac{S^k}{\tau_p}, \tag{8}$$

where R_{sp}^{k} is the spontaneous emission rate, given by $R_{\mathrm{sp}}^{k} = \sum_i U_{\mathrm{rad}}^{k,i}$. G_k^{mod} is the GS (ES) modal gain, β_{sp} is the spontaneous emission factor, and τ_p is the photon lifetime [31], which accounts for the intrinsic and mirror loss. The GS and ES modal gains are given by

$$\begin{aligned} G_k^{\mathrm{mod}} &= G_0^k \sum_i \Gamma_i(\rho_n^{k,i} + \rho_p^{k,i} - 1) \\ &= \underbrace{G_0^k \sum_i \Gamma_i \rho_n^{k,i}}_{G_k^{\mathrm{mod},n}} + \underbrace{G_0^k \sum_i \Gamma_i \rho_p^{k,i}}_{G_k^{\mathrm{mod},p}} - G_0^k \sum_i \Gamma_i, \end{aligned} \tag{9}$$

with $k = \mathrm{ES}, \mathrm{GS}$. The coefficient G_0^{GS} was estimated to be $\sim 433\ \mathrm{cm}^{-1}$ through a fitting of the measured modal gain versus current reported in Ref. [24] (see Fig. 4), resulting in $G_0^{\mathrm{GS}} \sum_i \Gamma_i \sim 52.4\ \mathrm{cm}^{-1}$, where $\Gamma_i \sim 2\%$. The coefficient G_0^{ES} has been set to $1.8 G_0^{\mathrm{GS}}$ to account for the ES degeneracy. Unless otherwise specified, the main simulation parameters employed in this work are summarized in Table 1. The separation between GS and ES energy levels is taken from Ref. [14] and corresponds to a difference in GS and ES recombination energy of 55 meV similar to the one reported in Ref. [16]. The QD shape, composition, and size as well as the InGaAs DWELL thickness significantly influence the QD electronic structure and therefore the escape rates out of the QD states. The less carriers escape out of the GS and ES, the less they are captured

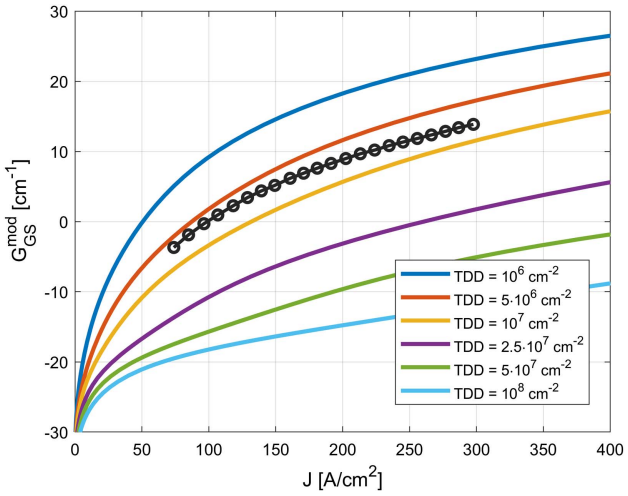

Fig. 4. Calculated GS modal gain versus current density for different levels of TDD and experimental gain (circles) from Ref. [24].

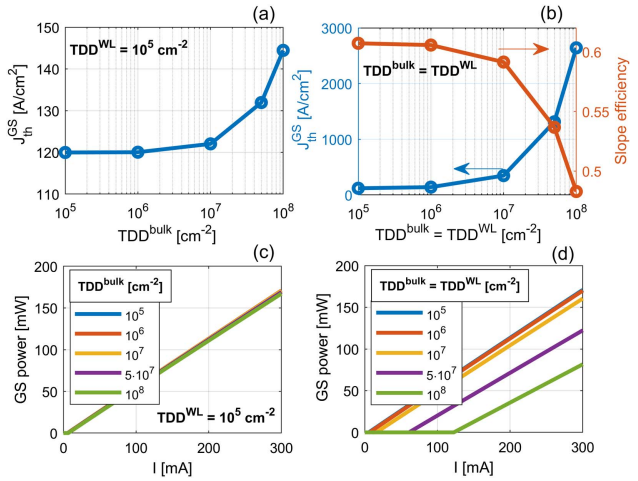

Fig. 5. (a) GS threshold current density and (c) optical power as a function of TDD^{bulk}, for fixed DWELL SRH lifetime corresponding to $TDD^{WL} = 10^5$ cm^{-2}. The solid lines are almost overlapped. (b) GS threshold current density and slope efficiency and (d) optical power as a function of TDD in the barrier and DWELL layers ($TDD^{WL} = TDD^{bulk}$).

by the TDs in the WL. Therefore, the DWELL and QD design provides further degrees of freedom for device optimization, e.g., to improve the insensitivity of QDs to threading dislocations. The values of carrier capture and relaxation times are in line with Ref. [26] where ultra-fast hole dynamics and picosecond or subpicosecond electron dynamics have been measured.

All the simulations assume isothermal conditions and ambient temperature.

3. RESULTS AND DISCUSSION

A. Impact of Threading Dislocations

We investigate the impact of SRH recombination due to TDs, both in the DWELL and barrier layers. Figure 4 shows the modal gain of the device under study for different TD density. In the TDD range 5×10^6–10^7 cm^{-2}, the calculated gain is similar to the experimental one reported in Ref. [24].

For a qualitative comparison with experimental results, we consider a Fabry–Perot laser with loss of $\alpha_m = 8.6$ cm^{-1} (corresponding to a Fabry–Perot cavity length $L = 1325$ μm), to guarantee lasing on the GS only [24].

To disentangle the impact of TDs in barrier and QW layers, Figs. 5(a) and 5(c) show simulation results when TDs are present in the barrier only, whereas Figs. 5(b) and 5(d) consider the more realistic situation of similar TD density in barrier and DWELL layers. The GS threshold current density [Fig. 5(a)] and the light–current characteristics [Fig. 5(b)] are marginally affected by TD-induced lifetime degradation in the barrier layers.

On the other hand, TD-mediated recombination in the DWELL affects the laser performance significantly. Figure 5(b) analyzes the threshold current density and slope differential efficiency as a function of TDD, taking into account SRH lifetime reduction according to Eq. (6) both in barrier and DWELL layers. The slope efficiency is defined as $(q/\hbar\omega)\cdot(dP/dI)$, with ω being the GS emission angular frequency, and it has been evaluated just above laser threshold. In this case, as the TD density in the DWELLs increases, the effective injection efficiency into the QDs diminishes, causing increased threshold current and reduced slope efficiency. This is also evident from the light–current characteristics in Fig. 5(d) calculated for different TDD values. Therefore, the TDs in the DWELL layers are those responsible for the degradation of the laser performance. Similar scaling of threshold current with TD density has been observed experimentally in Ref. [32], where devices of different generations having TDD density in the same range of Figs. 5(b) and 5(d), have been compared. These results also support the hypothesis that the degradation mechanisms limiting the long-term reliability could be correlated to a gradual propagation of TDs toward the quantum wells of the device active region [33].

B. Impact of Carrier Transport on Double-State Lasing and GS Power Quenching

In this section we discuss the influence on the CW performance of the asymmetry in the transport of electrons and holes across the barrier, owing to the different electron and hole low-field mobility in the GaAs layers. We demonstrate that this asymmetry is at the basis of the GS power quenching after the ES lasing threshold. For this purpose, we have set the mirror loss to $\alpha_m = 26.6$ cm^{-1} (corresponding to $L = 428$ μm). In this case, dual-state emission occurs at a reasonable ES threshold current. All results reported in this section are calculated for TDD $= 5 \times 10^6$ cm^{-2}.

Figure 6(a) shows the optical power emitted on the GS (solid) and ES (dotted) when the mobilities of electrons and holes in the SCH region are set to conventional room temperature values, corresponding to $\mu_n = 8500$ cm^2/(V · s) and $\mu_p = 350$ cm^2/(V · s). In this case, the GS power decreases as the current overcomes the ES threshold and it is completely quenched at sufficiently high currents. To highlight the impact of the unbalance of electron and hole mobility, Fig. 6(b) shows the GS (solid) and ES (dotted) optical power by forcing

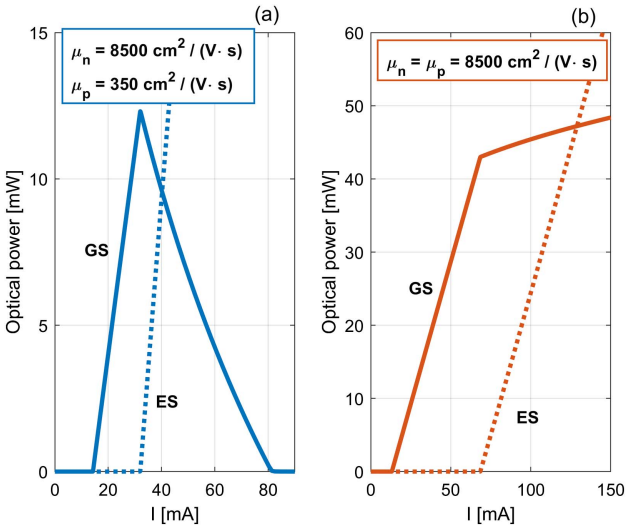

Fig. 6. GS (solid) and ES (dotted) optical power with (a) $\mu_n = 8500\ \mathrm{cm}^2/(\mathrm{V}\cdot\mathrm{s})$ and $\mu_p = 350\ \mathrm{cm}^2/(\mathrm{V}\cdot\mathrm{s})$ and (b) $\mu_n = \mu_p = 8500\ \mathrm{cm}^2/(\mathrm{V}\cdot\mathrm{s})$ in the SCH region.

$\mu_n = \mu_p = 8500\ \mathrm{cm}^2/(\mathrm{V}\cdot\mathrm{s})$. In this case, the GS power is not quenched when the ES turns on, demonstrating that the origin of quenching can be explained by the different mobilities. The same conclusions can be drawn forcing $\mu_n = \mu_p = 350\ \mathrm{cm}^2/(\mathrm{V}\cdot\mathrm{s})$ (not reported in this work), which only causes a larger separation between GS and ES threshold currents.

The asymmetry in the transport of electrons and holes is mirrored into the rate at which carriers are filling the various QD layers. This is emphasized in Fig. 7(a), showing the net capture rate of carriers from the bulk states to the WL with $\mu_n = 8500\ \mathrm{cm}^2/(\mathrm{V}\cdot\mathrm{s})$ and $\mu_p = 350\ \mathrm{cm}^2/(\mathrm{V}\cdot\mathrm{s})$. Each color corresponds to a different QD layer, with layer 1 (5) being the closest to the p-contact (n-contact). Layers located farthest from the p-contact are filled by holes at a smaller rate. On the contrary, if electron and hole mobilities are equal, holes are more evenly distributed and all the QD layers are filled at a similar rate, which increases linearly with the injected current. This is presented in Fig. 7(b), reporting the net capture rate of carriers from the bulk states to the WL with $\mu_n = \mu_p = 8500\ \mathrm{cm}^2/(\mathrm{V}\cdot\mathrm{s})$. This last case is in line with the exciton rate equation approach that, neglecting carrier transport and hole dynamics, was initially used to model double-state lasing in QDs [34]. Indeed the power–current characteristics in Fig. 6(b) well reproduce the results one would get in the exciton approximation [34], which is unable to reproduce the GS quenching. On the other hand, several experiments have shown that double-state lasing is often characterized by the GS quenching, as reproduced in Fig. 6(a) by our transport model with realistic material parameters. This provides a physical background for the results presented in Ref. [14] based on a phenomenological fitting parameter that was *ad hoc* introduced to mimic the asymmetric electron/hole transport. It is worth noticing that the onset of the GS quenching is characterized by an optical threshold. Varying the mirror loss in the asymmetric transport case, we have found that the reduction of the GS power after the ES threshold is observable only for $\alpha_m > 21\ \mathrm{cm}^{-1}$. On the contrary, for equal electron and hole mobilities, the GS power quenching never occurs whatever the value of α_m is.

In order to achieve deeper insight into the dual-state competition, it is convenient to inspect the overall, separate contributions of electrons ($G_{\mathrm{GS}}^{\mathrm{mod},n}$) and holes ($G_{\mathrm{GS}}^{\mathrm{mod},p}$) to the GS modal gain [see Eq. (9)]. For the sake of brevity, we only discuss explicitly the case with $\mu_n = 8500\ \mathrm{cm}^2/(\mathrm{V}\cdot\mathrm{s})$ and $\mu_p = 350\ \mathrm{cm}^2/(\mathrm{V}\cdot\mathrm{s})$. As the injected current grows between the GS and ES threshold currents, $G_{\mathrm{GS}}^{\mathrm{mod},n}$ decreases [see Fig. 8(a)] due to the spectral hole burning of GS electrons that are

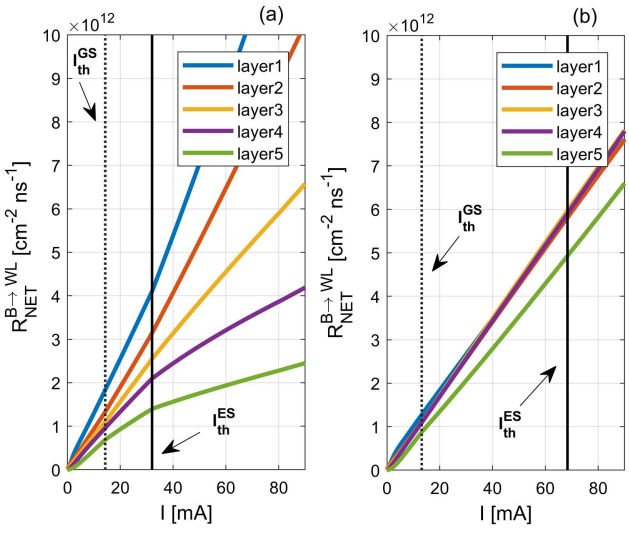

Fig. 7. Net capture rate from the bulk states to the WL with (a) $\mu_n = 8500\ \mathrm{cm}^2/(\mathrm{V}\cdot\mathrm{s})$ and $\mu_p = 350\ \mathrm{cm}^2/(\mathrm{V}\cdot\mathrm{s})$ and (b) $\mu_n = \mu_p = 8500\ \mathrm{cm}^2/(\mathrm{V}\cdot\mathrm{s})$ in the SCH region. Layer 1 (5) is the closest to the p-contact (n-contact).

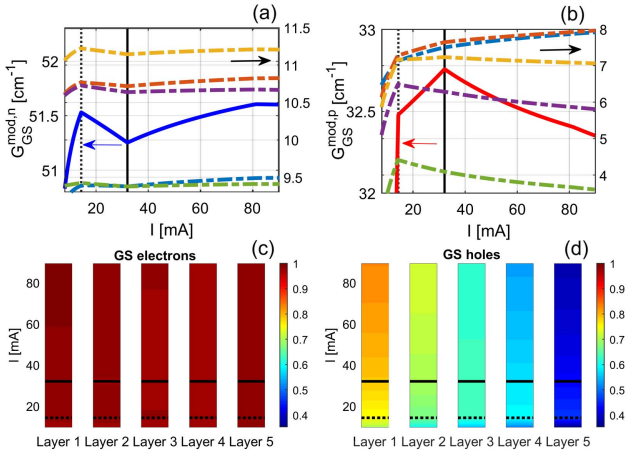

Fig. 8. Contribution of (a) electrons and (b) holes to the GS modal gain: solid line is the overall contribution, whereas colored dashed lines are the contribution of the different layers (color legend is the same as in Fig. 6). Vertical lines indicate GS and ES threshold currents. (c) GS electrons and (d) holes occupation probability. The mobility of electrons and holes in the SCH region is $\mu_n = 8500\ \mathrm{cm}^2/(\mathrm{V}\cdot\mathrm{s})$ and $\mu_p = 350\ \mathrm{cm}^2/(\mathrm{V}\cdot\mathrm{s})$. Layer 1 (5) is the closest to the p-contact (n-contact).

injected from the ES at a slower rate than they recombine. The electron gain compression due to spectral hole burning is compensated by the growth of hole gain to keep the lasing threshold gain. Indeed $G_{GS}^{mod,p}$ increases [see Fig. 8(b)], such that the GS modal gain remains clamped. The dashed curves in Figs. 8(a) and 8(b) quantify how electrons and holes of the various layers contribute to the overall gain. Only the GS holes of the two layers close to the p-side contribute with increasing gain, compensating for the gain reduction in all the other layers. In contrast, the hole gain contribution of layers far from p-side reduces as power increases because the slow hole transport prevents the refurbishment of holes lost due to stimulated emission. On the other hand, in the case of symmetric mobility $\mu_n = \mu_p = 8500\ \mathrm{cm^2/(V \cdot s)}$, we have found that the hole contribution is always increasing for any current injection. At the ES threshold current, the ES stimulated emission turns on and starts recombining the ES electrons and holes. This mechanism competes with the relaxation rate from the ES to the GS. Now the contribution of the GS holes is not enough to compensate for the electron spectral hole burning. As a consequence, the GS electron population has to increase such that $G_{GS}^{mod,n}$ can maintain the GS threshold condition. Then, the net transition rate of electrons from the ES to the GS decreases due to Fermi blocking; this rate balances the GS stimulated emission rate until the GS optical power is eventually quenched [14]. These trends are also supported by the electron and hole GS occupation probability of the various QD layers: as shown in Figs. 8(c) and 8(d), the GS is almost completely filled with electrons, whereas it is populated scarcely and unevenly by holes.

In summary, the reduction with increasing current of the hole gain contribution in the layers closer to the n-side is caused by the slow hole transport and it is therefore an additional mechanism, besides spectral hole burning, causing gain compression. Spatial hole burning or other gain compression effects are not directly included in the model, but could be taken into account by introducing a phenomenological compression factor parameter [31]. The accurate quantification of the effective gain compression coefficient requires, however, the simulation of the laser intensity modulation response which is out of the scope of this work [35].

C. Impact of p-Type Modulation Doping

In order to analyze the impact of modulation doping on dual-state emission, we set the mirror loss to $\alpha_m = 26.6\ \mathrm{cm^{-1}}$. All results reported in this section are calculated for TDD $= 5 \times 10^6\ \mathrm{cm^{-2}}$. In this context, the aim of p-type doping is reducing the GS threshold current and increasing the ES one such that the GS power is optimized. To focus on the role of doping in terms of electrostatics and transport, in the analysis we intentionally neglect possible additional loss due to free carrier absorption caused by the extra holes in the barrier. For the sake of the following analysis, it is worth noticing that the SRH lifetimes calculated according to Eq. (6), accounting for the doping dependence in dislocation free GaAs from Ref. [30], are dominated by the effect of the TDs.

Modulation doping is implemented by 10-nm-thick doped layers, with doping density N_A, placed as in Fig. 1. Figure 9 shows the optical power emitted on the GS (solid) and ES (dotted) with N_A equal to 0, $5 \times 10^{17}\ \mathrm{cm^{-3}}$, and $3 \times 10^{18}\ \mathrm{cm^{-3}}$, respectively. These doping levels correspond to 0, 10, and 60 extra holes per QD. Adding 10 extra holes per QD is beneficial, as the GS power quenching is cured and the GS threshold current is reduced. However, 60 extra holes turn out to be excessive, as the previous benefits are partially undermined. Figure 10(a) shows the GS (blue) and ES (red) threshold current density, J_{th}^{GS} and J_{th}^{ES} respectively, as functions of N_A. An optimum density of $5 \times 10^{17}\ \mathrm{cm^{-3}}$ exists, as this concentration minimizes J_{th}^{GS} and maximizes J_{th}^{ES}.

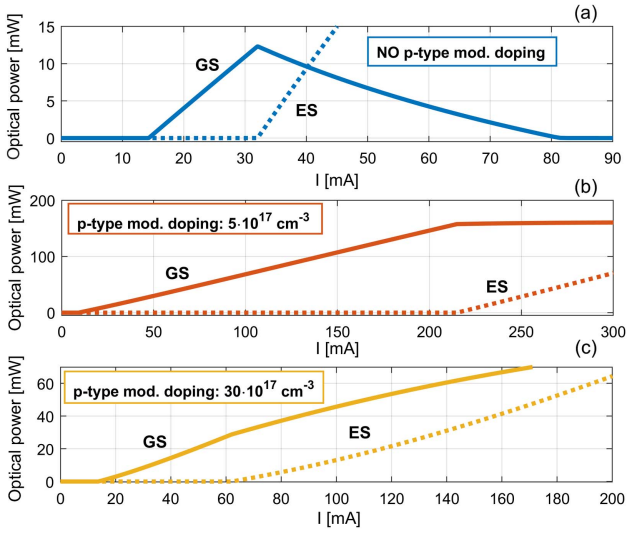

Fig. 9. GS (solid) and ES (dotted) optical power with (a) no p-type modulation doping and a p-type modulation doping of (b) $5 \times 10^{17}\ \mathrm{cm^{-3}}$ and (c) $30 \times 10^{17}\ \mathrm{cm^{-3}}$.

These results, showing an optimal doping density to minimize the GS threshold current, are consistent with the experiments in Ref. [20]. We have also verified that such optimum value is almost insensitive to the TDD value. In Ref. [20], it was speculated that the optimum results from a balance between the increase of gain enabled by doping and the increase

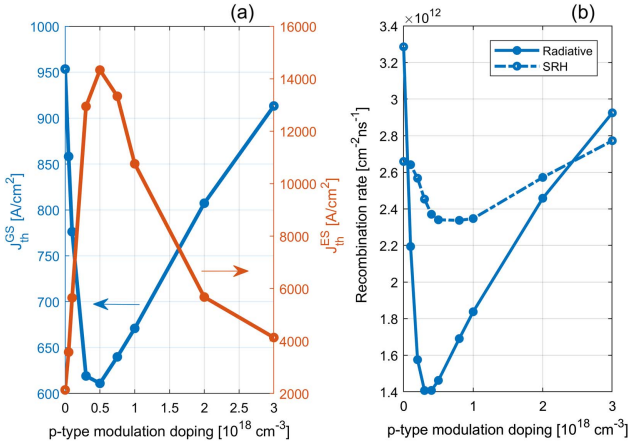

Fig. 10. (a) GS (blue) and ES (red) threshold current density as functions of the p-type modulation doping density. (b) Total radiative and SRH recombination rates as functions of p-type modulation doping density calculated at the J_{th}^{GS} values in (a).

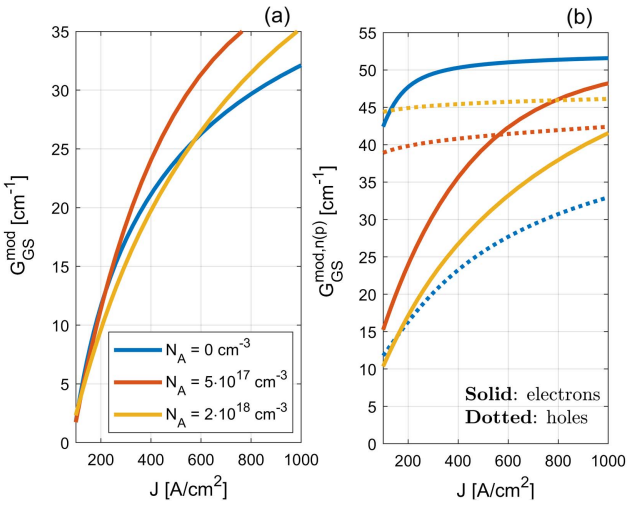

Fig. 11. (a) GS modal gain versus current density and (b) holes ($G_{GS}^{mod,p}$, dashed) and electrons ($G_{GS}^{mod,n}$, solid) contributions to the modal gain.

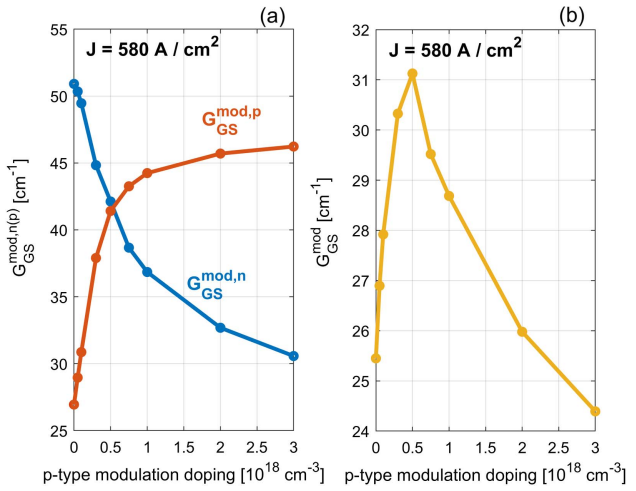

Fig. 12. (a) Contribution of electrons (blue) and holes (red) to the GS modal gain at $J = 580$ A/cm^2 versus p-doping density and (b) corresponding GS modal gain.

of doping-induced defects. However, the analysis of the integrated radiative and non-radiative recombination rates as a function of N_A reported in Fig. 10(b) demonstrates that the GS threshold minimum is strongly correlated to the doping dependence of the radiative recombination rate, whereas the influence of doping on the SRH recombination rate turns to be marginal. The optimum appears as an intrinsic consequence of a non-monotonic dependence of the modal gain on doping density: the increase of the hole modal gain contribution with N_A, due to the larger density of holes, is in fact counteracted at higher N_A values by a decrease of the electron modal gain contribution due to electrostatic effects.

We report in Fig. 11(a) the modal gain versus current density for three different doping levels N_A and in Fig. 11(b) the separate contributions of electrons and holes to the modal gain. While the hole contribution to the gain increases as expected for p-doping, we observe a decrease of the electron contribution to the GS gain that, to the best of our knowledge, has not been previously reported. The balance between the increased hole and reduced electron contributions makes the doped samples exhibit a higher or lower total gain—at fixed current injection—with respect to the undoped one. Long devices with low threshold gain (e.g., lower than 15 cm^{-1} in this example) could indeed not benefit too much from doping, since their threshold current would be higher in the doped case. This result may explain the anomalous increase of threshold current with doping recently reported in Ref. [36].

Figure 12(a) shows the electron and hole contributions to the GS modal gain, $G_{GS}^{mod,n}$ and $G_{GS}^{mod,p}$, respectively, as a function of N_A, at constant current density $J = 580$ A/cm^2. Since this value is smaller than the minimum GS threshold current density (see Fig. 10), the GS modal gain is not clamped for any of the considered doping levels. In addition, Fig. 12(b) shows the resulting GS modal gain. At low doping densities, the increase in $G_{GS}^{mod,p}$ outweighs the decrease in $G_{GS}^{mod,n}$, such that the GS modal gain grows. At $N_A = 5 \times 10^{17}$ cm^{-3}, the electron and hole contributions balance each other, maximizing the GS modal gain. At higher doping concentrations, the drop in $G_{GS}^{mod,n}$ is steeper compared to the growth in $G_{GS}^{mod,p}$ and the GS modal gain is diminished. Therefore, the existence of an optimum value appears to stem from the impact of p-type modulation doping on the GS modal gain at a given injected current.

To shed further light on this mechanism, we report in Fig. 13(a) the conduction band energy (solid) and electron quasi-Fermi level (dashed) for the bulk states of the SCH region at $J = 580$ A/cm^2 and for the same N_A values in Fig. 9. Notice that the multiple peaks observed in the QD stack region arise because of the electric field modulation caused by the depleted thin doped regions. As the doping concentration increases, the energy barrier which electrons injected from the

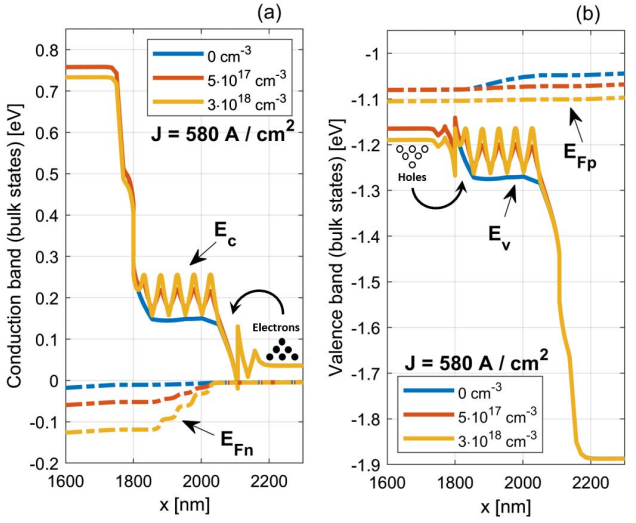

Fig. 13. (a) Conduction band (solid) and electron quasi-Fermi level (dashed) for the bulk states of the SCH region at $J = 580$ A/cm^2. (b) Valence band (solid) and hole quasi-Fermi level (dashed) for the bulk states of the SCH region at $J = 580$ A/cm^2.

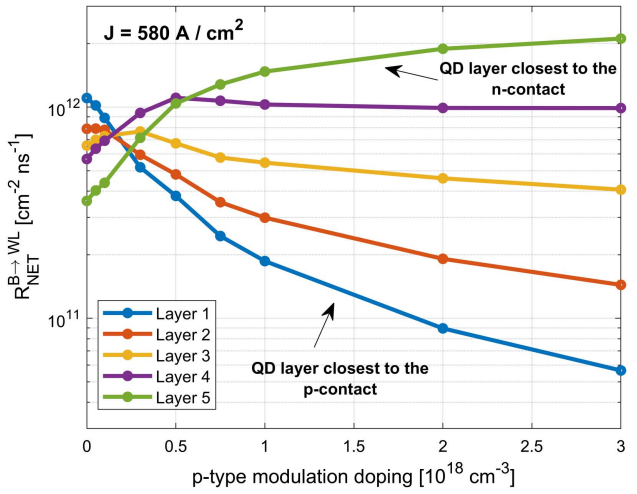

Fig. 14. Net capture rate from the bulk states to the WL at $J = 580$ A/cm^2 for each layer of QDs.

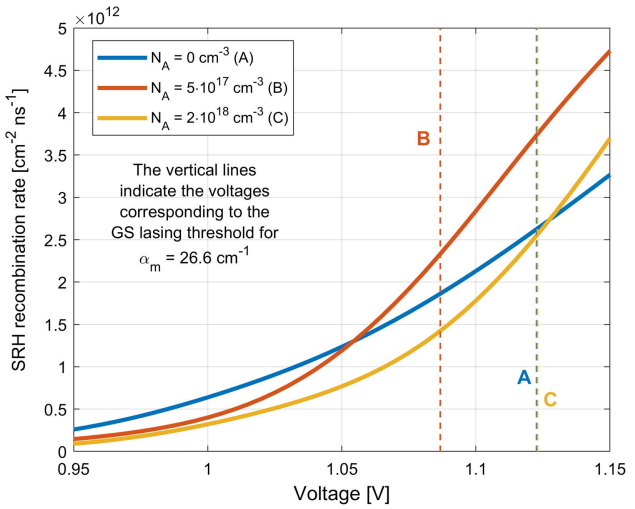

Fig. 15. Total SRH recombination rate versus voltage at three different doping levels. The vertical dashed lines indicate the voltage value corresponding to the lasing threshold.

n-contact have to overcome to reach the QD active layer region steadily rises. Concurrently, the electron quasi-Fermi level is pushed deeper in the energy gap. As a consequence, the bulk electrons in the active region diminish progressively, becoming unavailable to be captured by the QDs. Therefore, $G_{GS}^{mod,n}$ in Fig. 12(a) steadily decreases as the doping increases. On the other hand, the valence band (solid) and hole quasi-Fermi level (dashed) for the bulk states of the SCH region at $J = 580$ A/cm^2 are shown in Fig. 13(b). The energy barrier experienced by the holes injected from the p-contact is not significantly affected by N_A. Therefore, the change of hole density in the active region is directly related to the sole variation in the concentration of p-type dopants, which act as local source of extra holes. However, as doping grows holes almost entirely fill the GS, and the $G_{GS}^{mod,p}$ in Fig. 12(a) gradually saturates.

To corroborate this interpretation, we report in Fig. 14 for each QD layer the net capture rate of carriers from the bulk states to the WL (denoted by $R_{NET}^{B\to WL}$) at $J = 580$ A/cm^2. In the undoped case, the farther the QD layer is from the p-contact, the smaller $R_{NET}^{B\to WL}$ is. Indeed, while diffusing throughout the epitaxial structure upon injection from the p-contact, holes are progressively captured by the QD layers. As N_A grows, the electrostatic deformation of the band diagram reflects on $R_{NET}^{B\to WL}$. For doping levels higher than 10^{17} cm^{-3}, the closer the QD layer is to the n-contact, the larger $R_{NET}^{B\to WL}$ is. This signifies that most of the electrons injected from the n-contact are blocked by the energy barrier induced by the doping.

The influence of doping on carrier injection also has a significant influence on the dependence of the SRH recombination rate on injection conditions. As depicted in Fig. 15, at low voltages doping basically mitigates the (TD dominated) non-radiative recombination [22]. However, as carrier injection increases, non-radiative recombination in the doped samples starts to grow with a higher rate than it does in the undoped sample, owing to the higher hole density available in the DWELLs. The increase is larger at the intermediate doping level than at the highest one, because in the latter case electron injection from the n-contact is hindered by the energy barrier induced by the depleted delta-doped layers. Despite the marked difference in the voltage dependence of the SRH recombination rate, all the three samples present a similar amount of SRH recombination at the lasing thresholds, highlighting that the most relevant factor for the GS threshold minimization is the change of the radiative recombination rate, and therefore of the GS modal gain, with doping density.

4. CONCLUSIONS

This work has presented an investigation of the mechanisms limiting the performance of QD lasers epitaxially grown on silicon, on the basis of a transport model including QD carriers and photon rate equations. Overcoming the traditional lumped formulations based on rate equations, our approach can simulate the PIV characteristics of a dual-state lasing device starting from the description of materials, doping, and geometry. For bulk materials, consolidated measurement-based properties (e.g., mobility, bandgap, density of states) are available. For the QD material, electronic structure and characteristic carrier dynamics time constants can be extracted from literature devices representative of QD-on-Si technology, as done here, or calculated from first principle approaches. This enables applying the tool in the computer-aided design of the epitaxial structure, as a supporting tool in prototyping campaigns.

It is demonstrated how carrier transport and electrostatic effects are essential for catching and explaining the main static characteristics of these lasers. The analysis of the impact of threading dislocations in the barrier and DWELL layers on the lasing performance pinpoints a dominant effect of the TDs in the DWELL layers, supporting the hypothesis that long-term reliability issues suffered by these layers can be correlated to a thermally activated climbing of the TDs toward the active region. When accounting for transport mechanisms, double-state lasing and GS power reduction naturally emerge as a consequence of the inherently asymmetric transport of

electrons and holes, explaining the reason why conventional excitonic models cannot reproduce such an effect, and providing justification for the use in lumped rate equation models of phenomenological fitting parameters mimicking this effect. Finally, the physics behind p-type modulation doping and its effectiveness to minimize the GS threshold and maximize the ES/GS thresholds' ratio has been thoroughly investigated. The existence of an optimum doping level results from the competition between the doping-induced increase of hole modal gain contribution and the decrease of electron modal gain contribution, and therefore depends also on the threshold gain of the specific sample under study. If non-radiative carrier lifetime is dominated by threading dislocations, the impact of doping on the non-radiative recombination rate turns to be marginal with respect to the impact on the modal gain.

The presented model does not account for self-heating effects. While this could be a worthy extension of the present work, we expect that the overall scope of the presented results, which focus on next-to-threshold operating conditions, remains valid from a qualitative standpoint. In support of this, we remark that two-state lasing and GS quenching have been reported for both pulsating and continuous wave laser operation.

Disclosures. The authors declare no conflicts of interest.

REFERENCES

1. K. Nishi, K. Takemasa, M. Sugawara, and Y. Arakawa, "Development of quantum dot lasers for data-com and silicon photonics applications," IEEE J. Sel. Top. Quantum Electron. **23**, 1901007 (2017).
2. S. Chen, W. Li, J. Wu, Q. Jiang, M. Tang, S. Shutts, S. N. Elliott, A. Sobiesierski, A. J. Seeds, I. Ross, P. M. Smowton, and H. Liu, "Electrically pumped continuous-wave III-V quantum dot lasers on silicon," Nat. Photonics **10**, 307–311 (2016).
3. Y. Shi, Z. Wang, J. V. Campenhout, M. Pantouvaki, W. Guo, B. Kunert, and D. V. Thourhout, "Optical pumped InGaAs/GaAs nanoridge laser epitaxially grown on a standard 300-mm Si wafer," Optica **4**, 1468–1473 (2017).
4. A. Y. Liu and J. Bowers, "Photonic integration with epitaxial III-V on silicon," IEEE J. Sel. Top. Quantum Electron. **24**, 6000412 (2018).
5. J. Norman, M. J. Kennedy, J. Selvidge, Q. Li, Y. Wan, A. Y. Liu, P. G. Callahan, M. P. Echlin, T. M. Pollock, K. M. Lau, A. C. Gossard, and J. E. Bowers, "Electrically pumped continuous wave quantum dot lasers epitaxially grown on patterned, on-axis (001) Si," Opt. Express **25**, 3927–3934 (2017).
6. Y. Wan, J. Norman, Q. Li, M. J. Kennedy, D. Liang, C. Zhang, D. Huang, Z. Zhang, A. Y. Liu, A. Torres, D. Jung, A. C. Gossard, E. L. Hu, K. M. Lau, and J. E. Bowers, "1.3 μm submilliamp threshold quantum dot micro-lasers on Si," Optica **4**, 940–944 (2017).
7. A. Y. Liu, J. Peters, X. Huang, D. Jung, J. Norman, M. L. Lee, A. C. Gossard, and J. E. Bowers, "Electrically pumped continuous-wave 1.3 μm quantum-dot lasers epitaxially grown on on-axis (001) GaP/Si," Opt. Lett. **42**, 338–341 (2017).
8. D. Jung, J. Norman, M. J. Kennedy, C. Shang, B. Shin, Y. Wan, A. C. Gossard, and J. E. Bowers, "High efficiency low threshold current 1.3 μm InAs quantum dot lasers on on-axis (001) GaP/Si," Appl. Phys. Lett. **111**, 122107 (2017).
9. A. Y. Liu, S. Srinivasan, J. Norman, A. C. Gossard, and J. E. Bowers, "Quantum dot lasers for silicon photonics," Photon. Res. **3**, B1–B9 (2015).
10. J. M. Gérard, O. Cabrol, and B. Sermage, "InAs quantum boxes: highly efficient radiative traps for light emitting devices on Si," Appl. Phys. Lett. **68**, 3123–3125 (1996).
11. Z. Liu, C. Hantschmann, M. Tang, Y. Lu, J. Park, M. Liao, S. Pan, A. M. Sanchez, R. Beanland, M. Martin, T. Baron, S. Chen, A. J. Seeds, I. White, R. Penty, and H. Liu, "Origin of defect tolerance in InAs/GaAs quantum dot lasers grown on silicon," J. Lightwave Technol. **38**, 240–248 (2019).
12. A. Markus, J. X. Chen, C. Paranthoën, A. Fiore, C. Platz, and O. Gauthier-Lafaye, "Simultaneous two-state lasing in quantum-dot lasers," Appl. Phys. Lett. **82**, 1818–1820 (2003).
13. W. W. Chow and F. Jahnke, "On the physics of semiconductor quantum dots for applications in lasers and quantum optics," Prog. Quantum Electron. **37**, 109–184 (2013).
14. M. Gioannini, "Ground-state power quenching in two-state lasing quantum dot lasers," J. Appl. Phys. **111**, 043108 (2012).
15. V. V. Korenev, A. V. Savelyev, A. E. Zhukov, A. V. Omelchenko, and M. V. Maximov, "Analytical approach to the multi-state lasing phenomenon in quantum dot lasers," Appl. Phys. Lett. **102**, 112101 (2013).
16. H. Huang, J. Duan, D. Jung, A. Y. Liu, Z. Zhang, J. Norman, J. E. Bowers, and F. Grillot, "Analysis of the optical feedback dynamics in InAS/GaAs quantum dot lasers directly grown on silicon," J. Opt. Soc. Am. B **35**, 2780–2787 (2018).
17. P. M. Smowton and I. C. Sandall, "Gain in p-doped quantum dot lasers," J. Appl. Phys. **101**, 013107 (2007).
18. V. V. Korenev, A. V. Savelyev, M. V. Maximov, F. I. Zubov, Y. M. Shernyakov, M. M. Kulagina, and A. E. Zhukov, "Effect of modulation p-doping level on multi-state lasing in InAs/InGaAs quantum dot lasers having different external loss," Appl. Phys. Lett. **111**, 132103 (2017).
19. Q. Li, X. Wang, Z. Zhang, H. Chen, Y. Huang, C. Hou, J. Wang, R. Zhang, J. Ning, J. Min, and C. Zheng, "Development of modulation p-doped 1310 nm InAs/GaAs quantum dot laser materials and ultrashort cavity Fabry-Perot and distributed-feedback laser diodes," ACS Photonics **5**, 1084–1093 (2018).
20. Z. Z. Zhang, D. Jung, J. C. Norman, P. Patel, W. W. Chow, and J. E. Bowers, "Effects of modulation p doping in InAs quantum dot lasers on silicon," Appl. Phys. Lett. **113**, 061105 (2018).
21. M. Gioannini, A. P. Cédola, N. D. Santo, F. Bertazzi, and F. Cappelluti, "Simulation of quantum dot solar cells including carrier intersubband dynamics and transport," IEEE J. Photovoltaics **3**, 1271–1278 (2013).
22. A. P. Cédola, D. Kim, A. Tibaldi, M. Tang, A. Khalili, J. Wu, H. Liu, and F. Cappelluti, "Physics-based modeling and experimental study of Si-doped InAs/GaAs quantum dot solar cells," Int. J. Photoenergy **2018**, 7215843 (2018).
23. D. Gready and G. Eisenstein, "Carrier dynamics and modulation capabilities of 1.55-μm quantum-dot lasers," IEEE J. Sel. Top. Quantum Electron. **19**, 1900307 (2013).
24. D. Jung, Z. Zhang, J. Norman, R. Herrick, M. J. Kennedy, P. Patel, K. Turnlund, C. Jan, Y. Wan, A. C. Gossard, and J. E. Bowers, "Highly reliable low-threshold InAs quantum dot lasers on on-axis (001) Si with 87% injection efficiency," ACS Photonics **5**, 1094–1100 (2018).
25. D. Inoue, D. Jung, J. Norman, Y. Wan, N. Nishiyama, S. Arai, A. C. Gossard, and J. E. Bowers, "Directly modulated 1.3 μm quantum dot lasers epitaxially grown on silicon," Opt. Express **26**, 7022–7033 (2018).
26. I. O'Driscoll, T. Piwonski, C.-F. Schleussner, J. Houlihan, G. Huyet, and R. Manning, "Electron and hole dynamics of InAs/GaAs quantum dot semiconductor optical amplifiers," Appl. Phys. Lett. **91**, 071111 (2007).
27. A. Tibaldi, F. Bertazzi, M. Goano, R. Michalzik, and P. Debernardi, "Venus: a vertical-cavity surface-emitting laser electro-opto-thermal numerical simulator," IEEE J. Sel. Top. Quantum Electron. **25**, 1500212 (2019).
28. M. Yamaguchi, A. Yamamoto, and Y. Itoh, "Effect of dislocations on the efficiency of thin-film GaAs solar cells on Si substrates," J. Appl. Phys. **59**, 1751–1753 (1986).
29. C. Andre, J. Boeckl, D. Wilt, A. Pitera, M. L. Lee, E. Fitzgerald, B. Keyes, and S. Ringel, "Impact of dislocations on minority carrier electron and hole lifetimes in GaAs grown on metamorphic SiGe substrates," Appl. Phys. Lett. **84**, 3447–3449 (2004).
30. M. P. Lumb, M. A. Steiner, J. F. Geisz, and R. J. Walters, "Incorporating photon recycling into the analytical drift-diffusion model of high efficiency solar cells," J. Appl. Phys. **116**, 194504 (2014).

31. L. A. Coldren, S. W. Corzine, and M. L. Masanovic, *A Phenomenological Approach to Diode Lasers* (Wiley, 2012), Chap. 2, pp. 45–90.
32. D. Jung, R. Herrick, J. Norman, K. Turnlund, C. Jan, K. Feng, A. C. Gossard, and J. E. Bowers, "Impact of threading dislocation density on the lifetime of InAs quantum dot lasers on Si," Appl. Phys. Lett. **112**, 153507 (2018).
33. M. Buffolo, F. Samparisi, L. Rovere, C. De Santi, D. Jung, J. Norman, J. E. Bowers, R. W. Herrick, G. Meneghesso, E. Zanoni, and M. Meneghini, "Investigation of current-driven degradation of 1.3 μm quantum-dot lasers epitaxially grown on silicon," IEEE J. Sel. Top. Quantum Electron. **26**, 1900208 (2020).
34. A. Markus, J. X. Chen, O. Gauthier-Lafaye, J. Provost, C. Paranthoen, and A. Fiore, "Impact of intraband relaxation on the performance of a quantum-dot laser," IEEE J. Sel. Top. Quantum Electron. **9**, 1308–1314 (2003).
35. J. Duan, H. Huang, B. Dong, J. C. Norman, Z. Zhang, J. E. Bowers, and F. Grillot, "Dynamic and nonlinear properties of epitaxial quantum dot lasers on silicon for isolator-free integration," Photon. Res. **7**, 1222–1228 (2019).
36. J. C. Norman, Z. Zhang, D. Jung, C. Shang, M. Kennedy, M. Dumont, R. W. Herrick, A. C. Gossard, and J. E. Bowers, "The importance of p-doping for quantum dot laser on silicon performance," IEEE J. Quantum Electron. **55**, 2001111 (2019).